Pure Appl. Geophys. 179 (2022), 2501–2522

https://doi.org/10.1007/s00024-022-03028-6

Pure and Applied Geophysics

Climatology of Medium-Scale Traveling Ionospheric Disturbances (MSTIDs) Observed with GPS Networks in the North African Region

Temitope Seun Oluwadare,[1,2] Norbert Jakowski,[3] Cesar E. Valladares,[4] Andrew Oke-Ovie Akala,[5] Oladipo E. Abe,[6] Mahdi M. Alizadeh,[1,7] and Harald Schuh[1,2]

Abstract—We present for the first time the climatology of medium-scale traveling ionospheric disturbances (MSTIDs) by using Global Positioning System (GPS) receiver networks on geomagnetically quiet days (Kp $\leq$ 3) over the North African region during 2008–2016. The ionospheric Total Electron Content (TEC) were estimated from the dual-frequency GPS measurements, and the TEC perturbations (dTEC) data were derived from the estimated TEC data. We focused on the TEC perturbations (dTEC) associated MSTIDs and statistically analyzed its characteristics, occurrence rate, diurnal and seasonal behavior as well as the interannual dependence. The results show that MSTID is a local and seasonal dependence. The result reveals that occurrence of MSTIDs increases with solar activity. It also shows that MSTIDs predominantly propagates towards the South (equatorward). The MSTIDs event period is (12 $\leq$ period $\leq$ 53 min), while the dominant peak-to-peak amplitude is (0.08 $\leq$ amp $\leq$ $\sim$ 1.5 dTECU). The study also shows that the amplitude of MSTIDs is higher at the northwest (Lat: $\sim$ 32° N to $\sim$ 38° N, Long: $\sim$ 2° W to $\sim$ 15° W) when compared with northeast (Lat: $\sim$ 28° N to $\sim$ 38° N, Long: $\sim$ 23° E to $\sim$ 40° E), and the disturbance occurrence time is more frequent within the hours of (1200–1600 LT), and (1000—1400 LT) in December solstice at daytime for stations located in the northwest and northeast part of the African region, respectively. While at the nighttime, the MSTIDs also exhibits variability in disturbance occurrence time around (northwest: 2100–0200 LT) and (northeast: 1900-0200 LT) in June solstice, but get extended to March equinox during solar maximum (2014). The mean phase velocity in daytime MSTIDs is higher than the nighttime in every season, except during June solstice.

Keywords: MSTIDs, TEC perturbation, ionospheric irregularities, atmospheric gravity waves.

Abbreviations

MSTIDs	Medium-scale traveling ionospheric disturbances
GPS	Global Positioning System
AGW	Atmospheric gravity waves
TEC	Total electron content
dTEC	TEC perturbations
NNSS	Navy Navigation Satellite System
SuperDARN	Super Dual Auroral Radar Network
HF	High frequency
COSMIC	Constellation Observing System for Meteorology, Ionosphere, and Climate
RO	Radio occultation
OR	Occurrence rate
LEO	Low Earth orbit
CDAAC	COSMIC Data Analysis and Archive Center
DCB	Differential code biases
VTEC	Vertical TEC
SSA	Singular spectrum analysis
FFT	Fast Fourier transform
POR	Percentage occurrence rate
LT	Local times
UT	Universal time
DT	Daytime
NT	Nighttime
AMEC	Annual MSTIDs event count

[1] Institut für Geodäsie und Geoinformationstechnik, Technische Universität Berlin, Str. des 17. Juni 135, 10623 Berlin, Germany. E-mail: oluwa@gfz-potsdam.de; temitopeseun@yahoo.co.uk; m.alizadeh@email.com; schuh@gfz-potsdam.de

[2] German Research Centre for Geosciences GFZ, Telegrafenberg, 14473 Potsdam, Germany.

[3] Ionosphere Group, German Aerospace Center (DLR), Institute of Communications and Navigation, Kalkhorstweg 53, 17235 Neustrelitz, Germany. E-mail: Norbert.Jakowski@dlr.de

[4] W.B Hanson Center for Space Sciences, University of Texas at Dallas, Richardson, USA. E-mail: Cesar.Valladares@utdallas.edu

[5] Department of Physics, University of Lagos, Akoka, Yaba, Lagos, Nigeria. E-mail: aakala@unilag.edu.ng

[6] Physics Department, Federal University Oye-Ekiti, Oye, Nigeria. E-mail: oladipo.abe@fuoye.edu.ng

[7] Faculty of Geodesy and Geomatics Engineering, K.N. Toosi, University of Technology, Tehran, Iran.

1. Introduction

Medium-scale traveling ionospheric disturbance (MSTID) is one of the major and frequent ionospheric irregularity phenomena at the F region Mid-latitude which may degrade positioning systems (Hernández-Pajares et al., 2017), and it has been studied to have the ability to propagate over long distances (Frissell et al., 2014). MSTID has been described as wave-like perturbations of ionospheric plasma propagating in the ionosphere characterized by a wavelength, period and phase speed of 50–500 km, 12–60 min and 50–400 m/s, respectively (Grocott et al., 2013; Hocke & Schlegel, 1996; Ogawa et al., 1987). Within the last 6 decades, a lot of MSTIDs studies have been carried out by various researchers around the globe using different instruments and techniques to understand this irregular ionospheric behavior. To mention a few amongst many are: Ogawa et al. (1987) who investigated MSTIDs occurrence frequency using the U.S. Navy Navigation Satellite System (NNSS) in polar region at a 1000 km altitude during the disturbed geomagnetic condition. They concluded that there was no increase in MSTIDs occurrence under disturbed condition. Hernández-Pajares et al. (2006, 2012), Kotake et al. (2007), Valladares and Hei (2012), Jonah et al. (2016), Figueiredo et al. (2018a, 2018b), and Chen et al. (2019) carried out independent research of MSTIDs using GNSS receiver network at difference location, and they reported nearly the same results in terms of seasonal occurrences, but with slight differences in the propagation directions characteristics.

Several studies have thought MSTIDs to be caused by atmospheric gravity waves (AGWs) through convection activities in troposphere (Jonah et al., 2016; Tsuda et al., 2014), and in the thermosphere, mesosphere (Figueiredo et al., 2018a, 2018b). In addition, AGWs have also been proposed to be generated by the sunrise and sunset terminators (MacDougall et al., 2009a). AGWs are the most impactful waves that contribute to the dynamical nature of the upper atmosphere, and it is also an important energy transfer mechanism from troposphere into the stratosphere, mesosphere, and thermosphere (Yue et al., 2019). The nighttime MSTIDs characteristics were observed to be different from the daytime characteristics, they were found to be associated with increases in the F-region peak electron density altitude by Behnke (1979). However, Kelley and Miller (1997) reported that nighttime MSTIDs characteristic seems not to be consistent with classical theory of AGWs. Hence, they suggested that an electrodynamical force such as Perkins instability (PI) to be an important mechanism responsible for the generation of mid-latitude nighttime MSTIDs (Garcia et al., 2000; Perkins, 1973; Tsugawa et al., 2007). The required condition for PI mechanism to play out is that the preferred alignment of the MSTID wave-fronts is northwest-southeast in the Northern hemisphere, and that the MSTIDs typically propagate toward the equatorial region, that is, towards the southwest in the Northern hemisphere. However, the growth rate of the generative mechanism of PI is very low, and therefore would require additional seeding mechanism such as AGWs to augment the low PI growth rate which consequently yield MSTIDs development (Miller et al., 2014).

Huang et al. (1994) reported AGWs for driving the MSTIDs in the bottomside F region, hence enhancing the growth rate. There are also reports of electrodynamic coupling processes between F- and E-regions to boost the low PI growth rate to allow for the nighttime MSTIDs development (Cosgrove, 2004). In addition, Otsuka et al. (2007) in their nighttime MSTIDs study over Japan have reported that both nighttime MSTIDs and E-region irregularities exhibited wave-like structures with a northwest-southeast aligned wave front propagating southwestward, they suggested that the electrodynamical coupling between the Es layer and F-region plays a significant role in generating nighttime MSTIDs. Studies have been carried out to estimate the propagation direction characteristics of MSTIDs in order to aid the understanding of MSTIDs climatology and their properties (i.e. wavelength, velocity, TEC fluctuations), their seasonal, and solar cycle dependence (Ding et al., 2011; Kotake et al., 2007; Oinats et al., 2016). Kotake et al. (2007) presented two-dimensional maps of TEC perturbations showing daytime MSTIDs propagation over Southern California (in Northern hemisphere), and by visual assessment they reported MSTIDs passage with wave-fronts elongated

from the Northeast to the Southwest (i.e. MSTIDs propagating southeastward). Oinats et al. (2016) investigated MSTIDs observation over European-Asian sector during the 2013–2014 using radar data and they reported its characteristics, diurnal, solar cycle, and geomagnetic activity dependence.

Many studies have reported the regular and dynamic nature of the ionospheric TEC at different latitudes over the African region (Ouattara and Fleury, 2011; Ngwira et al., 2013; D'ujanga et al., 2016) under limited solar activity, and with much emphasis on the general local or regional characteristics of ionospheric irregularities. However, there is an important aspect of ionospheric irregularities which is yet to be reported on both local and regional scale over Africa. In recent years, with an improved study of long—term time series of characterization of ionospheric GPS-TEC under different geomagnetic conditions during 2009—2016 (Oluwadare et al., 2018), certain wave-like structures of ionospheric TEC were observed to be irregularities which vary in time and space. The characteristics of this irregular phenomenon are mostly associated with MSTIDs as described by ionospheric irregularity theories and experimental results from authors who have reported MSTIDs observations over different regions around the globe except for the African region, and these have created a huge gap in comparison of interregional MSTIDs characteristics.

Hence, for the first time, we present the climatology of MSTIDs over the North African region during the geomagnetic quiet days (i.e. Kp $\leq$ 3) for the period of 9 years (2008–2016). The primary aim is to present the MSTIDs observations derived from estimated TEC perturbation (dTEC), occurrence rate (OR), characteristics and occurrence mechanism. We also made use of temperature profile obtained from low earth orbit (LEO) satellite to observe possible indications of the AGWs passage for a selected day. A daytime two-dimensional dTEC map for a case of MSTIDs passage and the regional distribution of MSTIDs occurrence map is also presented.

2. *Data and Method*

MSTIDs have been observed and estimated during 2008–2016 using seven ground-based dual-frequency GPS receiver network stations majorly situated at Northern African, a mid-latitude region. The location of the stations is given in the Table 1 below. The entire seven GPS network stations are shown in Fig. 1.

The observation GPS data in RINEX format were obtained from the following FTP sites: ftp://data-out.unavco.org/pub/rinex/, http://www.afrefdata.org/ and ftp://www.station-gps.cea.com.eg/ALX2/, respectively. The GPS distribution is presented with red triangle with the corresponding ionospheric pierce point (IPP) trajectory (blue color curve) of the GPS satellites (Fig. 1). To avoid multipath effects and effect from the mapping function uncertainty from the data, an elevation cut-off angle greater than 35° (Bagiya et al., 2009; Valladares & Hei, 2012) was adopted. The low geomagnetic activity (i.e. Kp index $\leq$ 3) data used in this study were obtained from the GFZ German Research Centre for Geosciences, Indices of Global Geomagnetic Activity, Potsdam, Germany (ftp://ftp.gfz-potsdam.de/pub/home/obs/kp-ap).

Furthermore, we observed and extracted temperature profile data from the Sounding of the Atmosphere using Broadband Emission Radiometry (SABER) (http://saber.gats-inc.com/browse_data.php#).

Table 1

GPS receiver stations showing geographical coordinate values and geomagnetic latitude values

Station name	Geog. Lat	Geog. Lon	Geomag. Lat
RABT	33.99° N	6.85° W	37.4° N
TETN	35.56° N	5.36° W	38.6° N
IFR1	33.51° N	5.13° W	36.7° N
NOT1	36.88° N	14.91° E	36.5° N
ALX2	31.20° N	29.91° E	28.5° N
NICO	35.14° N	33.40° E	31.8° N
RAMO	30.60° N	34.76° E	27.1° N

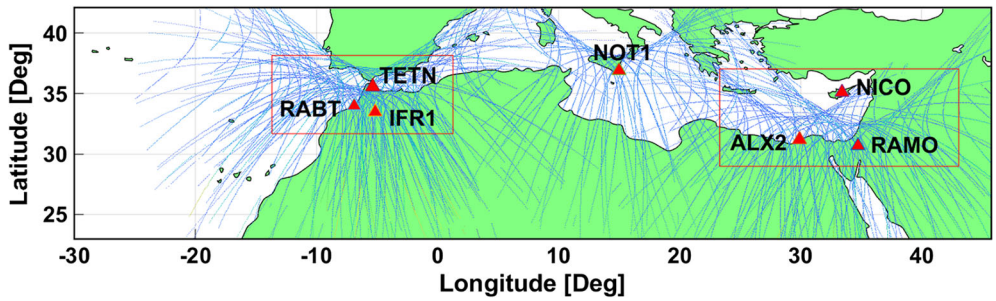

Figure 1
Location of the GPS receiver stations (red triangles) used in this study with an elevation mask $\geq 35^0$. GPS geometric networks were formed by choosing minimum of three stations (enclosed in red box) to form new sub networks (Northwest: RABT-TETN-IFR1, Northeast: ALX2-NICO-RAMO)

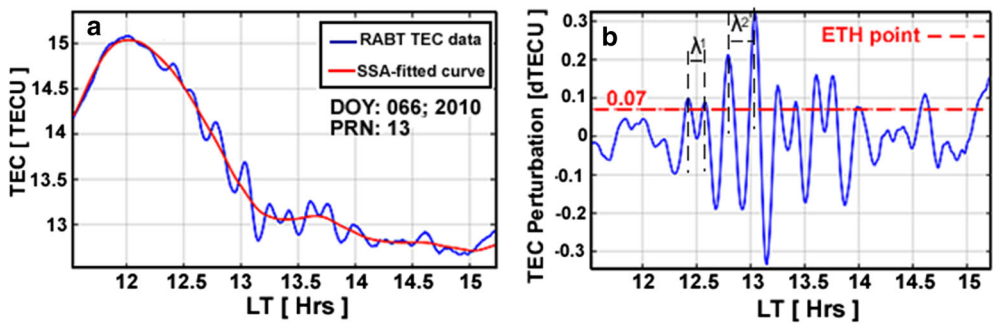

Figure 2
a TEC time series in PRN 13 as observed at RABT GPS station exhibiting wave-like structures depicting to be MSTIDs. The red line fitted curve ($TEC_{SSA\text{-}fit}$) is the background trend while **b** is the corresponding detrended TEC time series known as dTEC

3. *Estimation of Ionospheric GPS-TEC Derived*

The ionospheric Total Electron Content (TEC) was derived from Global Positioning System (GPS) measurements. The GPS-TEC derived was used to capture the Medium-Scale Traveling Ionospheric Disturbances (MSTIDs). TEC was computed using dual frequencies GPS receivers in which the first carrier frequency f_1 is centered at 1575.42 MHz and the second carrier frequency f_2 centered at 1227.60 MHz. Following Gao and Liu (2002), Zhao et al. (2009) and Abe et al. (2017), the code and carrier phase measurements obtained from GPS were used to compute the slant TEC (sTEC) along the signals path from the satellite to the receiver as follows:

$$sTEC_P = \frac{f_1^2 f_2^2}{40.3\left(f_1^2 - f_1^2\right)}\left[(P_2 - P_1) - (B_s + B_r + \varepsilon_P)\right] \quad (1)$$

$$sTEC_L = -\frac{f_1^2 f_2^2}{40.3\left(f_1^2 - f_1^2\right)}\left[(\lambda_2 L_2 - \lambda_1 L_1) - (\lambda_1 A_1 + \lambda_2 A_2 + \varepsilon_L)\right] \quad (2)$$

where P_1 is the code-delay measurement on frequency f_1 (m), P_2 is the code-delay measurement on frequency f_2 (m), B_s is the satellite differential code biases (m), B_r is the receiver differential code biases (m), L_1 is the carrier phase measurement on frequency f_1 (cycles), L_2 is the carrier phase measurement on frequency f_2 (cycles), A_1 is the ambiguity integer measure on the carrier phase on L_1 frequency (cycles), A_2 is the ambiguity integer measure on the carrier phase on L_2 frequency

(cycles), ε_p is the noise within the frequency channel and multipath associated with the code-delay measurements (m), ε_L is the noise and multipath associated with the carrier phase measurements (cycles), λ_1 and λ_2 are the wavelengths (m) corresponding to f_1 and f_2, respectively. The $sTEC_P$ obtained in Eq. (1) is continuous and unambiguous but noisy due to the frequency channel with a larger wavelength, pulse length of $\sim$ 300 m in free space while the $sTEC_L$ obtained in Eq. (2) is thinner (precise) but broken by sudden jumps and ambiguous due to the nature of the phase measurement, this results to cycle slips and many losses of lock (inability of the receiver to track the signals). The noisy but unambiguous $sTEC_P$ was used to level the $sTEC_L$ to arrive at a logical sTEC that is neither noisy nor ambiguous. As STEC is dependent on the ray path geometry through the ionosphere, it is needful to calculate an equivalent vertical TEC (VTEC) value which is independent of the elevation of the ray path. Hence, the VTEC is obtained by taking the projection from the slant to vertical using a mapping function M (θ) as contained in Klobuchar (1996), Mannucci et al. (1998), Ciraolo et al. (2007),

$$VTEC = STEC \times M(\theta) \tag{3}$$

$$M(\theta) = \frac{VTEC}{STEC} = \left[1 - \left(\frac{R_e \cos(\theta)}{R_e + h_{\max}}\right)^2\right]^{\frac{1}{2}} \tag{4}$$

where Re is the mean earth radius; 6371 km, θ = elevation angle of the satellite in degrees, h_{max} is the maximum height above the surface of the Earth, 350 km, has been taken to be h_{max} value, this is because at this height the ionosphere is assumed to be spatially uniform and simplified to be a thin layer, hence, this is considered as the height of maximum electron density at the F2 peak (Mannucci et al., 1998; Norsuzila et al., 2009). More details about VTEC estimation can be found in Mannucci et al. (1998) and Ciraolo et al. (2007). The background trends of the TEC time series were obtained by using singular spectrum analysis (SSA) with sliding window duration of 60 min and thereafter the output is subtracted from the original TEC time series resulting to TEC perturbation (dTEC), see Eq. (9) in the next section.

3.1. Fitting Tool: Singular Spectrum Analysis (SSA)

Different order of polynomial fittings as a bandpass technique to filter out diurnal variability and TEC perturbations associated with MSTIDs have been used in previous studies (Ding et al., 2004; Jonah et al., 2016; Valladares & Hei, 2012; Wang et al., 2007). However, most of these techniques have some limitations because the direction of the trend of the fitness line and degree of smoothness/resolution cannot be controlled due to imposition of predetermined function. This is the reason we adopted singular spectrum analysis (SSA) algorithm as a detrending tool for dTEC. Our choice of SSA (see Eqs. 5–8) among other things is because it is a nonparametric spectral estimation method for time series which cannot be affected by the limitations described above and most importantly due to its ability to find trends of different degrees of resolutions. We use Eqs. (5)–(8) to map the original one-dimensional TEC time series (i.e. FN) of length N into a multi-dimensional series of lagged vectors of size L, where N is greater than two. F implies TEC time series which formed a trajectory matrix (**F**), f_i implies TEC values at each epoch of each PRN as time increases.

$$\overbrace{f_1, f_2, f_3, \ldots f_L}^{window}, f_{L+1}, \ldots, f_N, \ implies \boldsymbol{F_1^T} = (f_1, f_2, f_3, \ldots f_L) \tag{5}$$

$$f_1, \overbrace{f_2, f_{3,4,3}, \ldots f_L, f_{L+1}}^{window}, \ldots, f_N, \ implies \boldsymbol{F_2^T} = (f_2, f_3, f_4, \ldots f_{L+1}) \tag{6}$$

$$f_1, f_2, \overbrace{f_3, f_4, f_5, \ldots, f_L, f_{L+2}}^{window}, \ldots, f_N, \ implies \boldsymbol{F_3^T} = (f_3, f_4, f_5, \ldots f_{L+2}) \tag{7}$$

$$F = [F_1, F_2, F_3, F_4 \ldots F_K] = \begin{pmatrix} f_1 & f_2 & f_3 & f_K \\ f_2 & f_3 & f_4 & f_{K+1} \\ f_3 & f_4 & f_5 & f_{K+2} \\ f_L & f_{L+1} & f_{L+2} & f_N \\ \vdots & \vdots & \vdots & \vdots \end{pmatrix}, \begin{cases} 1 < L < K \\ K = N - L + 1 \end{cases} \tag{8}$$

f_i must not be series of zeros, *i = 1,2 3,….L.* Golyandina et al. (2001) provides further details about SSA.

3.2. Estimation of TEC Perturbation (dTEC) and MSTIDs Event Threshold

An SSA fit is determined for each TEC time series ($TEC_{SSA\text{-}fit}$) of the corresponding satellite. The TEC perturbation (dTEC) is obtained by subtracting the $TEC_{SSA\text{-}fit}$ from the TEC estimate.

$$\mathrm{dTEC} = [\mathrm{TEC}] - [\mathrm{TEC}_{\mathrm{SSA-fit}}] \quad (9)$$

The approach to obtain dTEC in Eq. (11) is known as detrending. We determine that an MSTID event is detected whenever the TEC perturbation (dTEC) points fall above the event threshold (ETH) value of 0.07 TECU (Husin et al., 2011). The choice of ETH value was based on computing the standard deviation of the TEC perturbation (dTEC) of all epochs per observed satellite (Warnant, 1998; Warnant & Pottiaux, 2000). We iterated the entire standard deviation process for several satellites for different days and then found an approximate value of the most dominant standard deviation value which we set as the ETH point value.

3.3. Determination of MSTIDs Characteristics

In this study, we define MSTIDs as the dTEC that satisfy the following criteria: (1) the dTEC has as amplitude exceeding 0.07 TECU (1TECU = 10^{16} Electron/m^2) (Fig. 2b); (2) the horizontal wavelength is described as the distance between peak to peak of each wave event using visual assessment of dTEC signals and estimated to be less than 500 km. Lambda 1 (λ_1) and Lambda 2 (λ_2) indicated on Fig. 2b is for easy identification of wavelength; (3) the dTEC series was transformed from the time domain to the frequency domain in order to determine the event dominant period using a Fast Fourier Transform (FFT) (; Arikan & Yarici, 2017; Husin et al., 2011) and the period is estimated to be less than 60 min; (4) the propagation velocity does not exceed 450 m/s. The geometry of calculating the MSTIDs propagation parameters is plotted in Fig. 3b as an illustration in determining the azimuth and velocity. It must be noted that GPS receiver stations that are relatively close to each other are considered to form a sub-network (minimum of three stations) following the approach of Afraimovich et al. (1998), Hernández-Pajares et al. (2012), Valladares and Hei (2012), and Habarulema et al. (2013). Hence, we form a sub-network as seen in Fig. 1, where the GPS receiver station RABT, TETN and IFR1 is represented by X, Y and Z, respectively in Fig. 3a, b. We assume that the TID's wavefront propagates along the Earth's spherical surface and crosses point positions X, Y and Z with speed v and propagation azimuth (ϕ). The azimuth is measured from the north (**N**) towards the east along the horizon. The phase fronts propagation velocity satisfies the equations below (Ding et al., 2007).

$$V\Delta t_1 = \Delta S_1 \cos(\Phi - \psi_1),\ V\Delta t_2 = \Delta S_2 \cos(\Phi - \psi_2) \quad (10)$$

where Δt_1 and Δt_2 are time delays for dTEC to move from point X to Y and Z respectively along the Earth spherical surface and computed using cross-

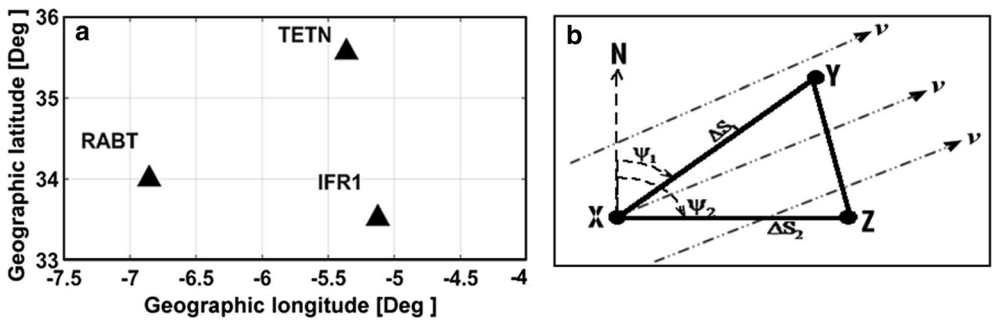

Figure 3
a An example illustrating one of the sub-networks (RABT-TETN-IFR1) used in studying MSTIDs characteristics [not to scale]. **b** the configured network geometry for obtaining the MSTIDs propagation direction and velocity

correlation. ΔS_1 is the spherical distances between X and Y, ΔS_2 is the spherical distance between X and Z, while ψ_1 and ψ_2 are the azimuths of spherical paths XY and XZ.

$$\Phi = \arctan\left(\frac{\Delta t_1.\Delta S_2.\cos\psi_2 - \Delta t_2.\Delta S_1.\cos\psi_1}{\Delta t_2.\Delta S_1.\sin\psi_1 - \Delta t_1.\Delta S_2.\sin\psi_2}\right) \tag{11}$$

Phase velocity of the TIDs was computed using

$$V = \frac{\Delta S_1}{\Delta t_1}\cos(\Phi - \psi_1) \tag{12}$$

Different observation points of X, Y, and Z were chosen to compute absolute values of V and Φ; thereafter we take the average value of V and Φ as the MSTIDs propagation velocity and azimuth. One important criterion that must be noted for computation of azimuth using Eq. (11) is that each of the GPS receiver stations within a sub-network must see the same satellite per observation time. Hence, the same satellite that could be seen by a sub-network is filtered for computation while other satellites are discarded. We also calculated the MSTIDs percentage occurrence rate (POR) of the event using Eq. (13).

$$\mathrm{POR} = \left[\frac{\alpha}{\omega}\right] \times [100] \tag{13}$$

where α is the total count number of dTEC estimation above ETH per epoch, ω is the total count number of dTEC estimation per epoch.

4. Results

We have analyzed the derived dTEC in the North African region during 2008–2016. The MSTIDs percentage occurrence rate (POR) and Variations in local time (LT) were analyzed by sorting the data into hourly bins. Following Jayawardena et al. (2016), we considered the daytime (DT: 0600–1800 LT) as dawn to dusk while the nighttime (NT: 1800-0600 LT) as dusk to dawn. For easy analysis and convenience, we converted the LT to universal time (UT) in a case where MSTIDs event are being observed simultaneously at more than one station in different sub-region. MSTIDs are observed and their characteristics are determined. Figure 4 shows an illustration for the case of a single day.

4.1. Observation of MSTIDs During 07 March 2010

In this section we determine the MSTIDs characteristics for 7th March 2010 (DOY 066) using Eqs. (10), (11), and (12). The TEC time series exhibited continuous fluctuations as observed in PRN 13 at different local times (LT) in different stations located within the same sub-region.

The TEC time series (TEC wave-like structures) in Fig. 4a has majorly been thought to be caused by AGW as stated in the introductory section. Figure 4b is the corresponding detrended TEC time series known as TEC perturbation (dTEC). In Fig. 4c, the minimum and maximum dominant period of MSTIDs is obtained using FFT and it is computed to be an average of 11.7 min and 18 min, respectively, while Fig. 4d shows that MSTIDs propagates towards the equator (southward) but indicated a higher percentage towards the south-east (SE).

Following Valladares and Hei (2012) and Jonah et al. (2016), the plotted TEC wave-like structure in Fig. 4a shows an indication of AGW passage, but Jonah et al. (2016) went further in the MSTIDs analysis by making use of temperature profile from COSMIC satellite and then extracted signature of upward propagation obtained from the detrended temperature profile which characterizes a possible passage of AGWs from the troposphere to the ionosphere, and which eventually propagate above 50 km into the ionosphere (Azeem & Barlage, 2017). However, the limitation with the COSMIC satellite temperature profile is its inability to capture temperature measurements above 60 km altitude. Hence further analysis was done to show the possibility that the AGWs propagated beyond 60 km, and this we have shown in Sect. 4.1.1.

4.1.1 Atmospheric Temperature Profile from the SABER Satellite Data During 07 March 2010

This section shows the possibility that the AGWs propagate beyond 60 km. Perturbed temperature data

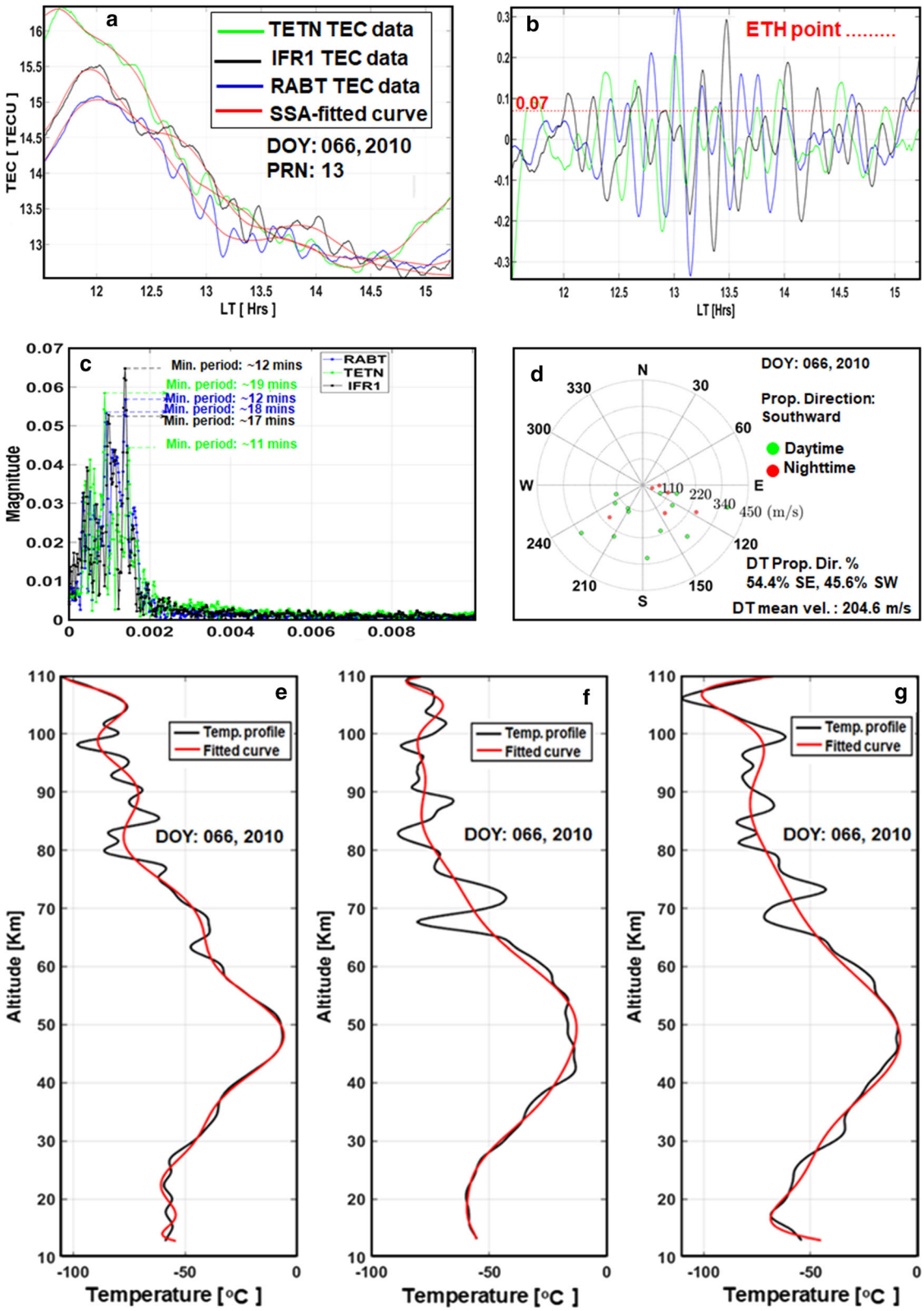
a
TETN TEC data
IFR1 TEC data
RABT TEC data
SSA-fitted curve
DOY: 066, 2010
PRN: 13
TEC [TECU]
LT [Hrs]
b
ETH point .....
0.07
LT [Hrs]
c
RABT
TETN
IFR1
Min. period: ~12 mins
Min. period: ~19 mins
Min. period: ~12 mins
Min. period: ~18 mins
Min. period: ~17 mins
Min. period: ~11 mins
Magnitude
d
DOY: 066, 2010
Prop. Direction:
Southward
Daytime
Nighttime
DT Prop. Dir. %
54.4% SE, 45.6% SW
DT mean vel. : 204.6 m/s
e
f
g
Temp. profile
Fitted curve
DOY: 066, 2010
Altitude [Km]
Temperature [°C]

◀Figure 4
a TEC versus UT measured by the GPS receivers (RABT, TETN and IFR1); color blue, green and black signal traces represent TEC values from the three receivers and the red lines represent the estimated background/unperturbed TEC values. **b** Corresponding detrended TEC time series of fig. (**a**), **c** MSTIDs minimum and maximum dominant periods, (d) polar plot representing MSTIDs velocities and azimuth for daytime during DOY 066. **e**–**g** Perturbed temperature profile from SABER satellite (black color) and its fit (red color). **h**–**j** Signature of upward AGW propagation obtained from the detrended temperature profile (**e**–**g**), and the prominent wavelength peak of the temperature profile during 1440–1445 UT (**k**–**m**). **n** The cross-section of the HWM zonal wind within the geographical location of the observed MSTIDs during 1440 to 1445 UT. The blue curve denotes a zonally averaged wind speed values at 400 km altitude, and the gray shading encloses the maximum and minimum values of zonal wind speed during this time

extracted from SABER satellite is shown in Fig. 4e–g.

The SABER data were filtered to obtain the temperature profile measurements within the geographic coordinates (lat: 28.07° N–37.07° N, long: 4.00° E–4.22° E) that are most aligned or close in distance to the geographic area of interest during 1440 to 1445 UT. We observed a considerable dynamic variation at a height between ∼ 30 and 100 km in each of the temperature profiles, indicating that the AGWs propagation survived up to 110 km altitude. With the current limitation of SABER satellite, our future investigation would require using instrument capable of capturing upper atmospheric observations above 110 km.

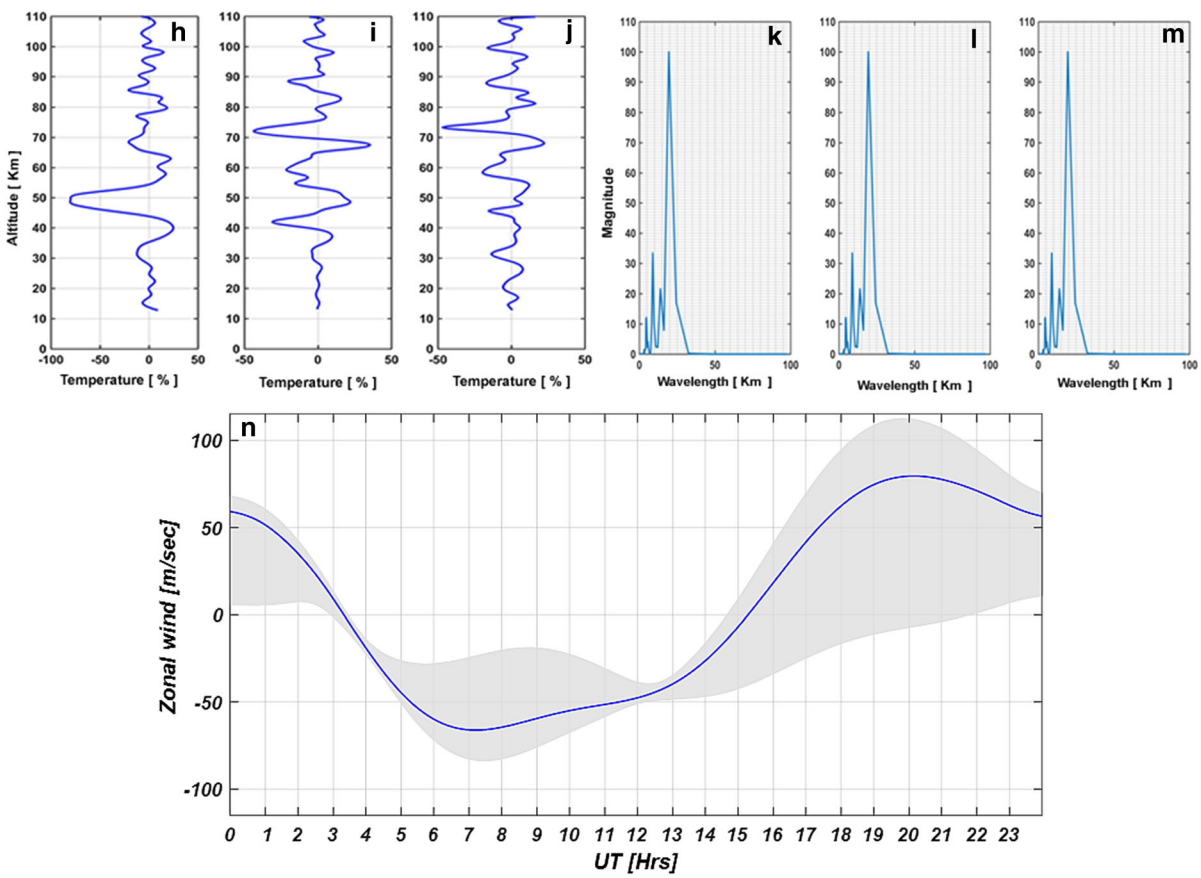

Figure 4
continued

Recently, reported cloud top brightness temperature which ranges between – 65 °C and – 20 °C corresponds to deep or strong convection activities as an important atmospheric parameter that exhibit the AGWs passage, and this temperature range feature could be observed in Fig. 4e–g. In the same vein, Fig. 4h–j shows the percentage of normalized temperature variations (% δT), where δT is the differences between the black and red curves in Fig. 4e–g. The power series with FFT was used to analyse the temperature profile and the wavelength of the gravity waves (Fig. 4k–m). Figure 4h shows a percentage temperature increase from ∼ ± 4% at 13 to 16 km to ∼ ± 22% at 68 km. Figure 4i shows from ∼ ± 3% at 26 to 31 km to ∼ ± 35% at ∼ 71 km, and Fig. 4j shows from ∼ ± 5% at 17 to 20 km to ∼ ± 22% at ∼ 72 km. This kind of altitude increase of change in temperature profile observed here can be interpreted as the vertical signature of AGWs propagation (Wang & Alexander, 2009). Figure 4k–m exhibits similar structural characteristics with prominent wavelength peaks of ∼ 20 km, 19.4 km, and 19.5 respectively.

Following Fritts and Alexander (2003), gravity waves with such amplitudes would survive up to the thermosphere region and then dispel energy in form of thermospheric body force**.** This is a possible source of the generation of MSTIDs (Vadas & Liu, 2009).

However, since there is no direct in-situ instrument collocated at the geographical area to measure the possibility of AGWs surviving beyond 110 km, we then made use of Horizontal Wind Model 2014 (HWM14). The HWM is an empirical model of the horizontal neutral wind in the upper thermosphere, and it describes the atmosphere's vector wind fields from the surface to around 450 km. It is based on wind data obtained from both ground based and space based instruments. Drob et al. (2015) provides further and more details about HWM.

The HWM zonal (west–east direction) winds around the geographic area of MSTIDs investigation for the selected day are shown in Fig. 4n a function of zonal wind speed (m/sec) values up to 400 km altitude and in UT. We use the HWM14 (Drob et al., 2015) to estimate the background neutral winds between 100 and 400 km. The model shows that the neutral wind drifted westward at pre-daytime at around 0400 UT, with the peak around 0600–0700 UT at daytime, and as time progresses from daytime to post daytime, it gradually drifted eastward again at around 1550 UT. Comparing the daytime southeastward propagation of MSTIDs in Fig. 4 of Sect. 4.1 with the neutral wind occurrence estimated using HWM14 in Fig. 4n, we could see that the dominant MSTID propagation direction agrees with the anti-wind direction at least for the selected period of investigation. This indicates that the observed MSTID was as a consequence of AGWs propagating in the thermosphere.

4.2. *Two-Dimensional Observation of MSTIDs Over North Africa*

Figure 5 shows the two-dimensional maps of MSTIDs over North Africa region at some selected times during 1000 to ∼ 1400 UT (daytime) of day 066, 2010, using PRN 13, 20 and 23 in all the stations. With careful observation, Fig. 5 shows an example of two-dimensional maps of TEC perturbations during the passage of MSTIDs over North African with maximum amplitude of 0.3 TECU. Due to a close intra-distance of the GPS receiver stations at the northwest sub-sector of Africa, we have chosen these stations for construction of MSTIDs 2D map.

Figure 5 shows a higher magnitude of MSTIDs at certain latitudes, this is in line with Abe et al. (2018)

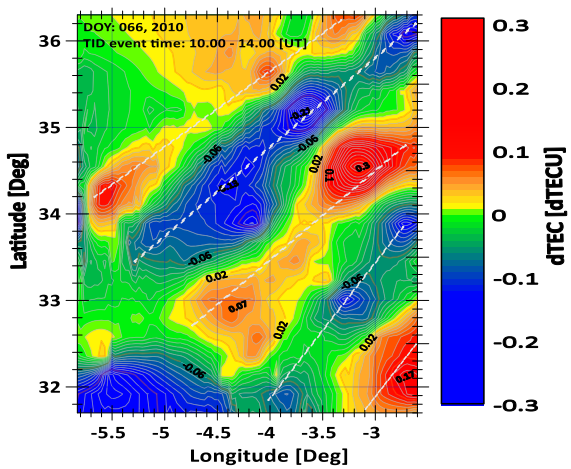

Figure 5
Two-dimensional maps of MSTIDs over North Africa at 1000 to ∼ 1400 UT on 7th March, 2010 (DOY 066).

longitudinal asymmetry of ionospheric irregularities over equatorial African. They showed in their studies that ionospheric irregularities are often frequent and are of higher magnitude in the western part of African equatorial region. The 2-D map showed that the MSTIDs band structures propagates towards south–east. The MSTID band structure peaks, and most especially the positive peaks seem to show an indication of south-eastward propagation as it gradually shifted from Lat. ∼ 34.6° to ∼ 32.4° (Long: ∼ − 5.5 ° to ∼ − 2.8 °).

4.3. *Local Observation of MSTIDs Over Selected GPS Receiver Stations in North Africa*

Figure 6a, b exhibits local diurnal and seasonal variations of MSTIDs occurrence at the different GPS receiver's stations located at mid-latitude stations. Data gap are indicated by the white portions of the Figure. Each station of the panel exhibited a similar contour structure but clearly shows different occurrence rate in terms of season and local time. In Fig. 6a, the MSTIDs occurrence shows a strong dependence on the season (June solstice) and local times but with a major peak around the (nighttime) 2100–0200 LT (∼ 27% to ∼ 45%). Also, the daytime MSTIDs exhibited some minor peaks in December solstice around 1200–1600 LT. In Fig. 6b, the nighttime MSTIDs occurrence exhibited similar seasonal (June solstice) and local times features as Fig. 6a but during 1900–0200 LT (∼ 25% to ∼ 40%). In addition, the daytime (09000–1600 LT) MSTIDs exhibited some peaks but not as pronounced as Fig. 6a during 2011 – 2015. The Fig. 6a, b show that both daytime and nighttime MSTIDs increase with an increasing solar activity. In Figs. 6a, b, the highest MSTID is consistently observed in June solstice (nighttime) during 2008—2016. The POR density shows that the occurrence rate varies with time of the day and season. This result seems to reveal MSTIDs occurrence variation and a level of inconsistency during day and night time from year to year. Hence, in subsequent section, we analyze day and nighttime amplitudes.

4.4. *Interannual and Seasonal Dependence of MSTIDs Amplitudes*

MSTIDs daily maximum amplitudes obtained from all stations at mid-latitude were analyzed in this section. Figure 7 shows MSTIDs daily maximum amplitudes for daytime and nighttime. For better visual analysis and to observe slightest changes in the multiple scatter plots, we introduced a mathematical function (simple moving average) which estimates the average value to determine the trend line-curve for both day and night (red and black line) which we use for analysis. Both nighttime and daytime exhibited similar pattern of trend curve but different amplitude variability. For instance, the nighttime amplitude consistently higher than daytime during the solar minimum year (2008–2010), having a high peak around (0.22—0.37 dTECU) in June solstice.

The high peak amplitudes switched from nighttime to daytime, exhibiting major peaks around (0.45–0.94 TECU) in September equinox during 2011–2015, and March equinox of 2014. The nighttime amplitude consistently exhibits higher peak during the June solstice, while the daytime consistently exhibits higher peak during the equinox months during 2008–2016. The dominant major higher peaks are observed in solar maximum year of 2014. By considering the solar minimum and maximum years, the nighttime amplitude seems to be slightly decreasing with increase in solar activity during June solstice. The daytime amplitude values increase with solar activity. However, it must be noted that the high background TEC exhibited during high solar activities in equinox season could also influence the high MSTIDs amplitude, in that whenever the TEC background is large, the amplitude of TEC perturbation is also large. Hence, this has in a way shown a correlation between background TEC and MSTIDs (Jonah et al., 2020).

4.5. *MSTIDs Characteristics*

In estimating the MSTIDs azimuth, we followed Eq. (11) in Sect. 3.3, and we choose to focus only on stations with the closest intra-distance (206 km) between one another (RABT-TETN-IFR1), while other stations having their intra-distance more than

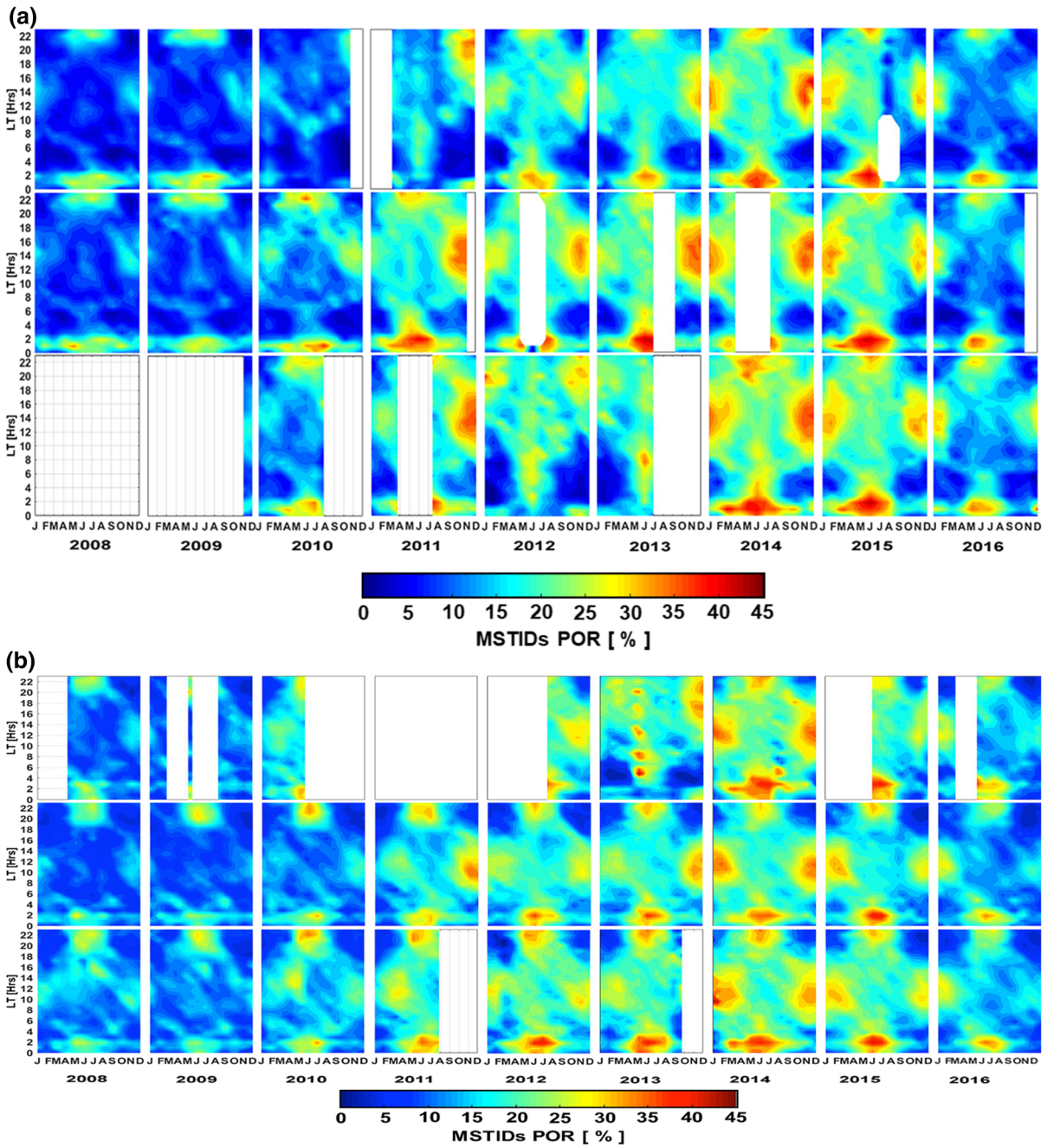

Figure 6

a Local diurnal and seasonal variations of MSTIDs occurrence in northwest (NW). White portions indicate data gap. Top panel is TETN station, Middle panel is RABT station, and bottom panel is IFR1. **b** Local diurnal and seasonal variations of MSTIDs occurrence in northeast (NE). White portions indicate data gap. ALX2 (top panel), NICO (Middle panel), and RAMO (bottom panel)

600 km are not considered. Figure 8 (top panel) shows polar plots representing MSTID velocities (in m/s) and azimuths during 2008—2016 for March equinox, June solstice, September equinox, and December solstice. In other to estimate a discrete propagation direction as a function of percentage

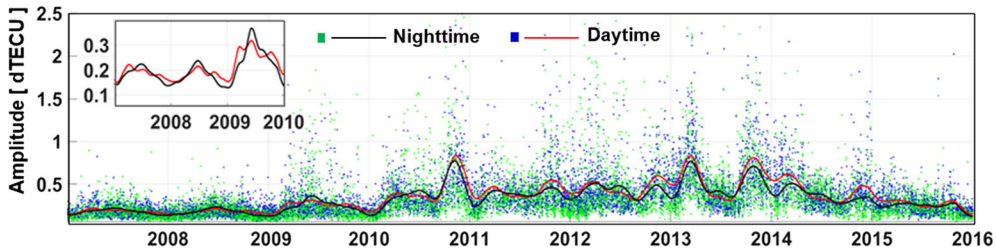

Figure 7
MSTIDs amplitude time series for both nighttime and daytime

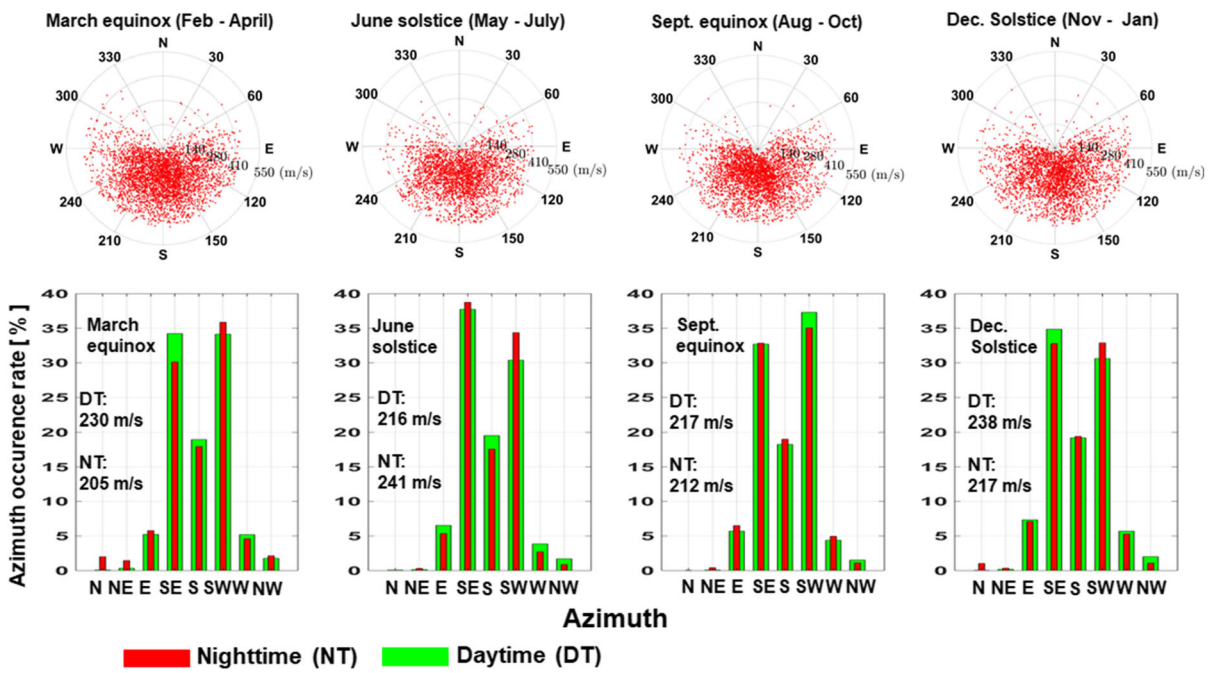

Figure 8
(Top panel) shows polar plots representing MSTID velocities (m/s) and azimuths for different seasons. (bottom panel) Bar chart showing cardinal directions of MSTIDs propagation having the percentage azimuth occurrence rate on the vertical axis, while the corresponding cardinal directions are on the horizontal axis

since the polar measurements looks clustered, and for clearer analysis, we further divided the azimuth measurements into daytime (DT) and nighttime (NT) and get it plotted on a bar-chart (Fig. 8 (bottom panel)).

The bar-chart shows discrete cardinal directions; North (N), North–East (NE), East (E), South–East (SE), South (S), South-West (SW), West (W), and North-West (NW) following Otsuka et al. (2013) approach, the bar chart also shows the daytime and nighttime mean velocity for each of the seasons. The MSTIDs propagation velocity is within 50—450 m/s, with velocity dominance of 200–300 m/s for every season except September equinox which has a dominance velocity value between 100 and 200 m/s.

Generally, the entire MSTIDs dominantly propagates southward (equatorward) as seen in Fig. 8 (top panel), dominantly between 120° and 230°. However, there are slight variations in propagation direction during daytime and nighttime as seen in Fig. 8 (bottom panel) which reveals the preferred propagation direction. Some few MSTIDs are observed to propagate northward, but most observation are seen to be dominantly southeastward and southwestward

for both daytime and nighttime MSTIDs in all the seasons but with slight exceptional cases in March equinox, June solstice and December solstice, where the nighttime MSTIDs propagation towards the southwest is slightly higher than the daytime by ∼ 1.80%, 4.01%, and 2.01%, respectively. Furthermore, both daytime and nighttime discretely propagated southward within 17–19% (azimuth occurrence rate) in all seasons, with the daytime slightly higher than the nighttime during the March equinox, and June solstice, respectively. On the other hand, the nighttime is slightly higher than the daytime during the September and December solstice, respectively. In addition, the daytime MSTIDs propagates towards the southeast, and slightly higher than the nighttime which also propagates in the same direction by ∼ 4.0%, and ∼ 3.0% during the March equinox, and December solstice, respectively. The nighttime MSTIDs percentage of propagation direction is higher in both southeast and southwest direction during June solstice. Also, during the September equinox, the daytime MSTIDs percentage of propagation direction is higher in southwest direction while the nighttime is slightly higher than the daytime in southeast direction. There are certain exceptions where the percentage of the southeastward propagation of daytime MSTIDs is comparable with that of the southwestward propagation during March equinox, the same thing also applies to nighttime MSTIDs but during December solstice. The detrended TEC time series were used to obtain the MSTIDs period by using fast Fourier transform (FFT) following (; Arikan & Yarici, 2017; Husin et al., 2011). The MSTIDs occurrence periods estimated with less than 6 min were regarded as noise fluctuations and therefore eliminated (Valladares and Hei, (2012)). The velocities were computed using Eq. (12) and the wavelengths were estimated from the distance the TEC wave-like structure traveled in space (latitude or longitude) following (Jonah et al., 2016). The daytime MSTIDs mean velocity is larger than the nighttime in all seasons, except in June solstice where the MSTIDs velocity experiences a reverse case. All seasons exhibited similar MSTIDs occurrence period (DT: 14—38 min, NT: 13—35 min) and wavelength (DT: 118–391 km, 96–382 km). The estimated values for velocity, period, and wavelength, respectively are within the ranges typically associated with MSTIDs discussed in Sect. 1. The regional distribution of MSTIDs on a spatio-temporal map over the mid-latitude of North Africa region is shown in Fig. 9. MSTIDs maps from different sectors at mid-latitude were superimposed.

The local time (LT) was converted to UT for time uniformity, easy analysis and most importantly to observe the dominant event time of occurrence for each year covering geographic latitudes (GL) 30–42° N and longitude 18° W–42° E (Otsuka et al., 2013).

The distribution of dominance occurrence of MSTIDs in Fig. 9 shows a semiannual variation with the major primary peak at June solstice (i.e. summer) during the NT (2100–0300 UT) and secondary peak at December solstice (i.e. winter) during the DT (1000–1500 UT). The maximum MSTIDs POR is observed to be ∼ 45% in 2014 and 2015.

5. Discussion

We have investigated statistically dTEC variations observed by GPS receivers located in Northern African region at mid-latitudes to reveal MSTIDs occurrence rate at local time, seasonal, latitudinal variations and propagation direction at daytime and nighttime, respectively, during 2008–2016. Our results show a distinct difference between the observed MSTIDs activity, and do not totally consistent with previous studies.

Figures 2a and 4a shows daytime TEC measurement exhibiting wave-like structures depicting to be MSTIDs. The TEC wave-like structures are similar to the TEC time series result obtained from Valladares et al. (2012) and Jonah et al. (2016). The observed MSTIDs could be possibly due to the passage of AGW. The AGWs passage involves vertical displacement of air parcels originating in the troposphere (Hines, 1960) and which causes perturbation in the ionospheric electron density. The neutral air wind perturbation collides with the plasma at F region, and then the charged ions are set in motion but are constrained to move along the magnetic field lines. The transportation of the charged molecules/ions along the magnetic field lines leads to electron density enhancement in certain places along the

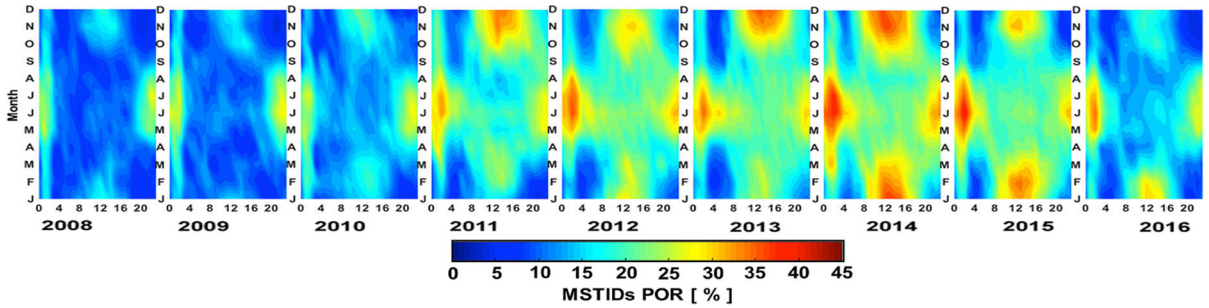

Figure 9
Universal time and seasonal variations in MSTIDs POR at mid-latitudes (42° N ≤ GL ≥ 30° N); 2008 – 2016

wave-front and also depletions in some other places. The continuous and regular enhancement and depletion of the plasma density consequently leads to TIDs occurrence (Hooke William, 1968), the explained process may be liable at the daytime MSTIDs occurrence in Figs. 2a and 4a. The event results shown in Fig. 4e–g, h–j, and k–m are similar to the results of Jonah (2017) where he observed and simulated the daytime MSTIDS occurrence over the equatorial and low latitude regions during strong tropospheric convection which builds up AGWs and possibly generates MSTID activities. He further reported that the prominent wavelength peaks in the range of 18 and 32 km are indications of AGWs activities on a strong tropospheric convection day, while prominent wavelength peaks which less than 10 km are indications of AGWs activities on a weak tropospheric convection day.

Following Jonah (2017), we may infer that the wavelength peaks ranging between 19.4 and ∼ 20 km obtained in Fig. 4 (k—m) could be an indication of convection activity occurrence on the selected day which is a potential source AGWs generation. Recently, Koucká et al. (2021) reported that AGWs propagating from the lower atmosphere up to the upper atmosphere could be either primary or secondary or even as tertiary waves. Earlier, Vadas and Nicolls (2012) in their study reported that AGWs which originate from the tropospheric height is capable of reaching the thermospheric height, and significantly create a perturbation in the wind and temperature profile, as observed in Fig. 4e–g. While the AGWs propagates upward, their amplitude grows exponentially as we can observe this in Fig. h–j between 30 and 80 km. Once the AGWs reach the amplitude saturation, they release their energy and momentum and this consequently influence the behavior and dynamics of atmosphere and also contribute to the development of TIDs (Trinh et al., 2018; Vadas and Liu 2012). At the mesospheric height (50–85 km), the primary gravity waves are generated, but about 80 km altitude, many primary gravity waves break at this level while some other primary waves (PWs) survived, but the survived PWs possesses small amplitude which cannot be captured by SABER satellite but still propagates upward. During this process of upward propagation of PWs, the secondary waves (SWs) are generated which then penetrate deeper into the thermosphere (Trinh et al., 2018). As indicated in Sect. 4.1.1, cloud top brightness temperature ranging between -65 °C and -20 °C are indications of deep convection activities that produce AGWs (Hoffmann et al., 2010). Hence, the observed MSTIDs on the selected day can be potentially caused by the surviving PWs or possibly generated SWs or both waves could possibly propagate further up to the thermosphere. Moreover, PWs propagate into the thermosphere under some favorable situation, and in fact most AGWs with convective sources get up to the thermosphere as higher order GWs and momentum is deposited. During this convective process, a local body forces are created which accelerate the neutral wind in the primary GWs direction, and also excites secondary GWs (Vadas & Liu, 2009; Vadas et al., 2014; Vadas and Azeem, 2021). However, in order to clearly ascertain which kind of the AGWs (primary or secondary or tertiary) that eventually penetrated beyond

110 km would require reverse ray tracing (Azeem, 2021), which is not within the scope of this study and can be considered separately in a future study. Further details regarding primary GWs and secondary GWs dynamics on reaching the thermosphere during convection process has been reported by Vadas and Azeem (2021).

The 2-D map in Fig. 5 seems to show MSTIDs band structure propagating from the northwest towards the northeast with a maximum amplitude peak value of 0.30 dTECU. The MSTID band structure peaks, and most especially the positive peaks seem to show an indication of south-eastward propagation as it gradually shifted from Lat. $\sim$ 34.6° to $\sim$ 32.4° (Long: $\sim -5.5°$ to $\sim -2.8°$).

Figure 6a, b illustrate the diurnal and seasonal variation of MSTIDs of GPS receiver stations located at northwest and northeast, respectively, with respect to local time. The Figures show different characteristics between daytime and nighttime MSTIDs occurrence, such as local effect, seasonal, and solar activity dependence. These facts indicate that different mechanisms initiate MSTIDs occurrence during daytime and nighttime period, and at different seasons. A high occurrence rate of MSTIDs was observed in the daytime during 1100–1600 LT, and 0900–1400 LT at northwest and northeast, respectively during the March equinox and December solstice, respectively. However, the nighttime MSTIDs exhibited highest occurrence rate observed in June solstice during $\sim$ 2100–0200 LT and $\sim$ 1900–0200 LT at northwest and northeast, respectively. In the current study, the magnitude of MSTIDs generally increases with increase in solar activity (Essien et al., 2021; Oinats et al., 2016). Our MSTIDs seasonal occurrence results show a larger part of agreement with the MSTIDs investigation conducted by Tsugawa et al. (2006) who reported MSTIDs occurrence over South-East Asian sector (Japan). In their investigation, they reported nighttime (2100–0300 LT) MSTIDs to be the highest activities in every year during summer (May–August), and daytime (0900–1500 LT) MSTIDs occurrence is also high during the winter, their result is similar with the current study. The slight difference between this current study and Tsugawa et al. (2006) is that the current study shows a clear increase in daytime MSTIDs occurrence as solar activity increases, but Tsugawa et al. (2006) reported that there is no clear indication of solar activity dependence of the daytime activities. They added that the summer nighttime activities become weaker as the solar cycle approaches its maximum which is however not so in this study. Furthermore, the seasonal results in this current study is similar to the result obtained from with MSTIDs study over the North American sector (California) conducted by Hernández-Pajares et al. (2012), they reported daytime MSTIDs occurrence during winter (November–January) and fall (August–October), and nighttime during summer (May–July) and spring (February–April), whereas this current study majorly report daytime and nighttime occurrence during December solstice and June solstice, respectively, and the nighttime (000 –0200 LT) slightly extends to March equinox season during the solar maximum of 2014.

In Fig. 7, each year of the MSTIDs amplitude time series exhibited an asymmetric structure, and most especially during the daytime period. The MSTIDs occurrence exhibited a significant increase in the year 2011 relative to 2009—2014, during September equinox, possibly due to the increase in solar activity as expressed by an increase in sunspot numbers. The mean sunspot numbers in September equinox in 2009, 2010, 2011, 2012, 2013, and 2014 are 4.9, 33.2, 104, 88, 87, and 109, respectively (see. http://www.sidc.be/sunspot-data/). Generally, the MSTIDs amplitude increase with an increase in solar activity, this result agrees with Oinats et al. (2016) who investigated MSTIDs observation over Hokkaido East during 2007—2014, and over European-Asian sector during the 2013–2014 using radar data. They reported an increase in amplitude with an increase in solar activity, and that the amplitude tends to increase with increasing auroral electrojet (AE) index, and also found that MSTIDs amplitude is dominantly high at daytime. The increasing MSTIDs with increase in solar activity in the current result also agrees with Essien et al. (2021) where they reported a long-term study of MSTIDs occurrence rate during 2014–2019 over South American equatorial region (Lat: 0°–15° S and Long: 30°–55° W). They concluded that MSTIDs increases with increasing solar activity.

In this study, MSTIDs propagation having the percentage azimuth occurrence rate below 20% exhibited in the bar chart (Fig. 8—bottom panel) are regarded insignificant, hence they are not considered. Previously, MSTIDs studies have been carried out in Northern hemisphere (NH), for example; Kotake et al. (2007) observed MSTID over Southern California using GPS network, and they reported that the azimuth during the daytime is southeastward in equinox and in winter season. They also reported the nighttime MSTIDs to be propagating southwestward and westward in equinox and summer seasons. Jacobson et al. (1995) investigated MSTIDs occurrence using a very long baseline interferometer (VLBI) array over New Mexico (35.9° N, 106.3° W), and they reported the preferred daytime MSTIDs propagation direction to be southward during winter and in equinox seasons. Furthermore, Ding et al. (2011) reported a dominant propagation of daytime MSTIDs towards the south (equatorward), and that the nighttime MSTIDs dominantly propagated southwestward in all seasons. Our result in the current study shows a similarity to those observed in the NH, in terms of seasonal propagation but slightly differs in propagation direction. The current daytime MSTIDs propagate generally towards the south (equatorward) (Fig. 8—top panel), but dominantly propagates southeastward in March equinox and December solstice, even though the daytime exceeded the nighttime by $\sim 4\%$. The daytime equatorward propagation is explained below. Thome (1964) stated that the most supported theory for propagation direction is that TIDs propagates in the direction of the geomagnetic field lines. Hooke William (1968, 1970) in his investigation on ionospheric response to internal gravity waves stated that at F-region heights, the ions move and travel along the geomagnetic field lines through neutral-ion collision, with a velocity the same as the velocity of the neutral motion along the geomagnetic field caused by the gravity waves, during this process some azimuthal directions of wave propagation are preferred as a function of the ionospheric response that are evoked. However, the motion of the ions across the magnetic field line is constrained to move along the magnetic field lines because the gyro-frequency of the ions is much higher than the frequency of the ion-neutral collisions. The direction of the motion of the ions consequentially leads to directivity in the response of the electron density variations to the gravity waves. This kind of directivity phenomena could be a contributor to daytime MSTIDs southward propagation direction (Kotake et al., 2007). Besides, an anisotropic frictional ion drag force has been thought as a possible candidate responsible for the southward propagation of the daytime MSTID direction (Kelley & Miller, 1997; Yeh & Liu, 1969).

The nighttime MSTIDs over the African NH dominantly propagates southwestward during March equinox, June solstice, and December solstice. The night MSTIDs also exhibits a slight similarity with the seasonal propagation dominance obtained by to Kotake et al. (2007), and Ding et al. (2011), except for December solstice. The nighttime MSTIDs has been thought to be generated Perkins instability (PI) (Perkins, 1973). The main concept of the Perkins instability (PI) is that when a perturbation of Pedersen conductivity (Σ) has a structure extended from Northwest to Southeast, and electric current $\mathbf{J}$ flowing Northeastward traverses the Pedersen conductivity perturbation. In this condition, the polarization electric field which is Northeastward (Southwestward) in the regions of low (enhanced) Pedersen conductivity is generated to maintain a divergence-free current. The generated polarization electric field (∂E) moves the plasma upward (downward) via the $E \times B$ drift, which consequently causes perturbation in the plasma density (Otsuka et al., 2013), and the mechanism for generating polarization electric field (∂E) is mostly consistent with an ionospheric instability mechanism introduced by Perkins (1973), but since PI growth rate is too small to initiate an appreciable amount of nighttime MSTIDs, it is generally accepted that some additional seed is needed to augment the low Perkins growth rate to allow for the development of MSTIDs. Gravity waves has been reported as a plausible candidate for driving nighttime MSTIDs in the bottomside F region, thus enhancing their growth rate (Huang et al., 1994). This process is a possible mechanism for generating the nighttime MSTIDs with phase fronts elongated from Northwest-Southeast in the NH. Therefore, the nighttime MSTIDs observed to be propagating southwestward over

North Africa region could be possibly caused by the electrodynamical force processes discussed above.

However, it is noteworthy to state that there are some nighttime MSTIDs observations in terms of seasons and propagation direction in the current study that are different from previous studies which is an indication that PI theory does not play out in some nighttime propagation. This indirectly means that not all of the nighttime MSTIDs observed in the Northern hemisphere are heading in the Perkins phase front normal direction. Distinctively in the current study, the dominant nighttime MSTIDs propagation direction during June solstice is observed to exhibit the highest peak of percentage azimuth occurrence rate but propagated southeastward, and also noticeable is the dominant daytime MSTIDs propagation direction during September equinox is observed to be southwestward, and about 17% to 19% of the daytime and nighttime MSTIDs discretely propagates southward in all seasons. These propagation direction behaviors are not similar with Kotake et al. (2007) and Ding et al. (2011). However, similar unconventional propagation direction behavior of MSTIDs have been reported. For instance, Figueiredo et al. (2018b) investigated the nighttime MSTIDS morphology over Cachoeira Paulista at Brazil in Southern hemisphere using Optical Thermosphere Imagers, and they reported certain class of nighttime MSTIDs to have propagated towards the northwestward direction in which they explained its mechanism as a consequences of Perkin instability theory, and another class of nighttime MSTIDs to have mainly propagated towards the north-northeastward direction. Also, in the same vein, Paulino et al. (2016) observed that nighttime MSTIDs over "São João do Cariri" in the Southern hemisphere exhibited a wide propagation direction towards the north, northeast, northwest, and southeast.

Hence, comparison of the nighttime MSTIDs propagation direction results from Kotake et al. (2007), Figueiredo et al. (2018b), Paulino et al. (2016), and the current study, does not totally align with one another. This shows that for this kind of situation, the PI does not play out at all instances of nighttime propagation. In addition, this is an indication that location of different MSTIDs source could possibly influence propagation direction as a mechanism that can determine the propagation direction of MSTIDs, and this could be a likely situation of the current study in Africa NH. Another reason for this propagation direction behavior could be as a result of atmospheric gravity waves and that the wind filtering mechanism which could possibly be operating effectively (Otsuka et al., 2011). More in-situ instrument may be needed in the future to further investigate the dynamics of propagation direction in the NH.

The mean propagation velocity of MSTIDs varies from 205 to 241 m/s, with the daytime propagation velocity mostly higher than nighttime, which is similar with previous study (Husin et al., 2011; Hernández-Pajares et al., 2012), except in June solstice where the nighttime is higher than the daytime. The higher nighttime propagation velocity in June solstice agrees with Oinats et al. (2016). The major contrast between present study and Oinats et al. (2016) is that, the higher nighttime MSTIDs propagation velocity value only happens in June solstice, whereas Oinats et al. (2016) reported a consistent higher nighttime propagation velocity values over the daytime during 2007–2014, using high-frequency (HF) radar data. Fig. (9) illustrates the general view of MSTIDs in the north Africa region and most importantly the MSTIDs occurrence dominance. In general, Figs. 6 and 9 show that MSTIDs maximize during the nighttime (2000–0400) UT of June solstice, followed by daytime (0900–1600) UT December solstice and minimizes at equinoxes in all the stations used. In addition, Figs. 6 and 9 have clearly revealed the progression in the growth rate of MSTIDs with increase of solar activity which agrees with Oinats et al. (2016) and Essien et al. (2021) as stated earlier. The MSTIDs maximizes at 2014, the peak of solar activity of solar cycle #24 and minimizes at 2008, the beginning of the minimum year of the cycle. The same occurrence mechanism discussed above for local sector is also responsible for the regional distribution. The figure shows a consistent increase in MSTIDs occurrence with increase solar activity.

6. Conclusions

For the first time, the climatology of MSTIDs has been studied during solar cycle #24 (2008-2016) using the GPS network within the North African sector at the Northern Hemisphere. Quiet days with Kp $\leq$ 3 were considered. We examined the MSTIDs occurrence rate and its characteristics for daytime and nighttime. We categorized MSTIDs into two groups based on location, Northwest (NW) and Northeast (NE). The study concluded that:

1. MSTIDs occurrence rate is majorly localized and seasonally dependent. It is more frequent at northwest compared with northeast. The daytime MSTIDs at NW and NE frequently occur around ($\sim$ 1200—$\sim$ 1600 LT) and ($\sim$ 1000 to $\sim$ 1400 LT) in December solstice, respectively. The nighttime MSTIDs frequently occur around (NW: 2100–0200 LT) and (NE: 1900–0200 LT) in June solstice, and exhibited a pronounced minor peak in solar maximum year (2014) during March equinox.
2. MSTIDs are more of solstice seasons phenomenon in both nighttime and daytime compared with equinoctial seasons. The solstice diurnal asymmetry was predominant at nighttime (daytime) in June solstice (December solstice) in comparison with equinoctial seasons.
3. MSTIDs propagation velocity is faster during daytime compared to nighttime, except in June solstice where the propagation velocity exhibited a higher magnitude at nighttime than daytime.
4. The magnitude of the MSTIDs occurrence depends on solar activities. MSTIDs maximizes (minimizes) during high (low) solar activity in both nighttime and daytime.
5. MSTIDs generally propagates equatorward (southward) for both daytime and nighttime, but dominantly propagates southwestward at nighttime.
6. On a regional distribution scale, MSTIDs activity exhibits a primary peak during June solstice and secondary peak during December solstice.

Acknowledgements

The authors thank the International GNSS Service (IGS), University NAVSTAR Consortium (UNAVCO), The Centre d'Etudes Alexandrines, Egypt, The African Geodetic Reference Frame (AFREF), and Constellation Observing System for Meteorology, Ionosphere, and Climate (COSMIC) for preserving the raw data and make it available for scientific uses. We also acknowledge the financial support from ADVANTAGE project (grant number: ZT-0007) funded by Helmholtz-Gemeinschaft, Germany.

Author contributions OTS performed data processing, MSTIDs estimation, MSTIDs statistical analysis, discussed the MSTIDs mechanisms and drafted the manuscript. NJ and CEV guided on MSTIDs mechanism and propagation direction respectively. AOA, OEA, MMA, Harald Schuh participated in the interpretation of the MSTIDs results, proper use of technical language and sequential arrangement of manuscript text structure. All authors have contributed to the work of OTS.

Funding

Open Access funding enabled and organized by Projekt DEAL. This work was financially supported by the Advance Technologies for Navigation and Geodesy (ADVANTAGE) project (grant number: ZT-0007) funded by Helmholtz-Gemeinschaft, Germany.

Availability of data and materials

The datasets generated and/or analyzed in support of the findings of this study are available upon request from the corresponding author.

Declarations

Competing interests The authors declare that they have no competing interests.

References

Abe, O. E., Otero Villamide, X., Paparini, C., Radicella, S. M., & Nava, B. (2017). Rodríguez-Bouza M (2017) Performance Evaluation of GNSS-TEC Estimation Techniques at the Grid Point in Middle and Low Latitudes during Different Geomagnetic Conditions. *Journal of Geodesy, 91*, 409–417. https://doi.org/10.1007/s00190-016-0972-z

Abe, O. E., Rabiu, A. B., & Radicella, S. M. (2018). Longitudinal Asymmetry of the occurrence of the plasma ionospheric irregularities over African low latitude region. *Journal of Pure and Applied Geophysics*. https://doi.org/10.1007/s00024-018-1920z

Afraimovich, E. L., Palamartchouk, K. S., & Perevalova, N. P. (1998). GPS radio interfereometry of travelling ionospheric disturbances. *Journal of Atmospheric and Solar Terrestrial Physics, 60*, 1205–1223.

Arikan, F., & Yarici, A. (2017). Spectral investigation of traveling ionospheric disturbances: IONOLAB-FFT. *Geodesy and Geodynamics., 8*(2017), 297–304. https://doi.org/10.1016/j.geog.2017.05.002

Azeem, I. (2021). Spectral asymmetry of near-concentric traveling ionospheric disturbances due to Doppler-shifted atmospheric gravity waves. *Frontiers in Astronomy and Space Sciences, 8*, 690480. https://doi.org/10.3389/fspas.2021.690480

Azeem, I., & Barlage, M. (2017). Atmosphere-ionosphere coupling from convectively generated gravity waves. *Advances in Space Research*. https://doi.org/10.1016/j.asr.2017.09.029

Bagiya, M. S., Joshi, H. P., Iyer, K. N., Aggarwal, M., Ravindran, S., & Pathan, B. M. (2009). TEC variations during low solar activity period (2005–2007) near the Equatorial Ionospheric Anomaly Crest region in India. *Annales Geophysicae, 27*, 1047–1057.

Behnke, R. (1979). F layer height bands in the nocturnal ionosphere over Arecibo. *Journal of Geophysical Research, 84*, 974–978. https://doi.org/10.1029/JA084iA03p00974

Chen, G., Zhou, C., Liu, Y., Zhao, J., Tang, Q., Wang, X., & Zhao, Z. (2019). A statistical analysis of medium-scale traveling ionospheric disturbances during 2014–2017 using the Hong Kong CORS network. *Earth, Planets and Space*. https://doi.org/10.1186/s40623-019-1031-9

Ciraolo, L., Azpilicueta, F., Brunini, C., Meza, A., & Radicella, S. M. (2007). Calibration errors on experimental slant total electron content (TEC) determined with GPS. *Journal of Geodesy, 81*, 111–120. https://doi.org/10.1007/s00190-006-0093-1

Cosgrove, R. B. (2004). Coupling of the Perkins instability and the sporadic E layer instability derived from physical arguments. *Journal of Geophysical Research*. https://doi.org/10.1029/2003JA010295

Ding, F., Wan, W., Ning, B., & Wang, M. (2007). Large-scale traveling ionospheric disturbances observed by GPS total electron content during the magnetic storm of 29–30 October 2003. *Journal of Geophysical Research*. https://doi.org/10.1029/2006ja012013,2007

Ding, F., Weixing, W., Guirong, X., Tao, Y., Guanlin, Y., & Jing-Song, W. (2011). Climatogy of medium-scale traveling ionospheric disturbances observed by a GPS network in central China. *Journal of Geophysical Research*. https://doi.org/10.1029/2011JA016545

Ding, F., Yuan, H., Wan, W., Reid, I. M., & Woithe, J. M. (2004). Occurrence characteristics of medium-scale gravity waves observed in OH and OI nightglow over Adelaide (34.5°S, 138.5°E). *Journal of Geophysical Research Atmospheres*. https://doi.org/10.1029/2003JD004096

Drob, D. P., Emmert, J. T., Meriwether, J. W., Makela, J. J., Doornbos, E., & Conde, M. (2015). An update to the Horizontal Wind Model (HWM): The quiet time thermosphere. *Earth and Space Science, 2*(7), 301–319. https://doi.org/10.5194/angeo-32-773-2014

D'ujanga, F.M., Opio, P., Twinomugisha, F. (2016). Variation of the totalelectron content with solar activity during the ascending phase of solarcycle 24 observed at Makerere University, Kampala. In: Fuller-Rowell, T., Yizengaw, E., Doherty, P.H., Basu, S. (Eds.), *Ionospheric space weather: longitude and hemispheric dependences and lower atmosphere forcing*. USA: Wiley. https://doi.org/10.1002/9781118929216.ch12.

Essien, P., Figueiredo, C. A. O. B., Takahashi, H., Wrasse, C. M., Barros, D., Klutse, N. A. B., Lomotey, S. O., Ayorinde, T. T., Gobbi, D., & Bilibio, A. V. (2021). Long-term study on medium-scale traveling ionospheric disturbances observed over the South American Equatorial Region. *Atmosphere, 12*, 1409. https://doi.org/10.3390/atmos12111409

Figueiredo, C., Takahashi, H., Wrasse, C. M., Otsuka, Y., Shiokawa, K., & Barros, D. (2018a). Medium-scale traveling ionospheric disturbances observed by detrended total electron content maps over Brazil. *Journal of Geophysical Research: Space Physics, 123*, 2215–2227. https://doi.org/10.1002/2017JA025021

Figueiredo, C. A. O. B., Takahashi, H., Wrasse, C. M., Otsuka, Y., Shiokawa, K., & Barros, D. (2018b). Investigation of nighttime MSTIDS observed by optical thermosphere imagers at low latitudes: Morphology, propagation direction, and wind filtering. *Journal of Geophysical Research: Space Physics, 123*, 7843857. https://doi.org/10.1029/2018JA025438

Frissell, N. A., Baker, J., Ruohoniemi, J. M., Gerrard, A. J., Miller, E. S., Marini, J. P., West, M. L., & Bristow, W. A. (2014). Climatology of medium-scale traveling ionospheric disturbances observed by the midlatitude blackstone superdarn radar. *Journal of Geophysical Research: Space Physics, 119*(9), 7679–7697. https://doi.org/10.1002/2014JA019870

Fritts, D. C., & Alexander, M. J. (2003). Gravity wave dynamics and effects in the middle atmosphere. *Reviews of Geophysics, 41*(1), 1003. https://doi.org/10.1029/2001RG000106

Gao, Y., & Liu, Z. Z. (2002). Precise ionosphere modeling using regional GPS network data. *Journal of Global Positioning Systems, 1*, 18–24.

Garcia, F. J., Kelley, M. C., Makela, J. J., & Huang, C. S. (2000). Airglow observations of mesoscale low-velocity traveling traveling ionospheric disturbances at mid-latitudes. *Journal of Geophysical Research, 105*, 18407–18415.

Golyandina, N., Nekrutkin, V., & Zhigljavsky, A. A. (2001). *Analysis of time series structure: SSA and related techniques*. Chapman and Hall.

Grocott, A., Hosokawa, K., Ishida, T., Lester, M., Milan, S. E., Freeman, M. P., Sato, N., & Yukimatu, A. S. (2013). Characteristics of medium-scale traveling ionospheric disturbances observed near the Antarctic Peninsula by HF radar. *Journal of Geophysical Research, Space Physics*. https://doi.org/10.1002/jgra.50515

Habarulema, J. B., Katamzi, Z. T., & McKinnell, L. A. (2013). Estimating the propagation characteristics of large-scale traveling ionospheric disturbances using ground-based and satellite data. *Journal of Geophysical Research, 118*, 7768–7782.

Hernández-Pajares, M., Juan, J. M., & Sanz, J. (2006). Medium-scale traveling ionospheric disturbances affecting GPS measurements: Spatial and temporal analysis. *Journal of Geophysical Research, 111*, A07S11. https://doi.org/10.1029/2005JA011474

Hernández-Pajares, M., Juan, J. M., Sanz, J., & Aragón-Àngel, A. (2012). Propagation of medium scale traveling ionospheric disturbances at different latitudes and solar cycle conditions. *Radio Science, 47*, RS0K05. https://doi.org/10.1029/2011RS004951

Hernández-Pajares, M., Wielgosz, P., Paziewski, J., Krypiak-Gregorczyk, A., Krukowska, M., Stepniak, K., Kaplon, J., Hadas, T., Sosnica, K., Bosy, J., Orus-Perez, R., Monte-Moreno, E., Yang, H., Garcia-Rigo, A., & Olivares-Pulido, G. (2017). Direct MSTID mitigation in precise GPS processing. *Radio Science, 52*, 321–337. https://doi.org/10.1002/2016RS006159

Hines, C. O. (1960). Internal atmospheric gravity waves at ionospheric heights. *Canadian Journal of Physics, 38*, 1441–1481.

Hocke, K., & Schlegel, K. A. (1996). Review of atmospheric gravity waves and travelling ionospheric disturbance: 1982–1995. *Ann. Geophysicae.*, *14*, 917–940. https://doi.org/10.1007/s00585-996-0917-6.

Hoffmann, L., & Alexander, M. J. (2010). Occurrence frequency of convective gravity waves during the North American thunderstorm season. *Journal of Geophysical Research*. https://doi.org/10.1029/2010JD014401

Hooke William, H. (1968). Ionospheric irregularities produced by internal atmo-spheric gravity waves. *Journal of Atmospheric and Terrestrial Physics, 30*, 795–823.

Hooke William, H. (1970). The ionospheric response to internal gravity wave. *Journal of Geophysical Research, Space Physics, 75*(28), 5535–5544.

Huang, C. S., Miller, C. A., & Kelley, M. C. (1994). Basic properties and gravity wave initiation of the mid-latitude F region instability. *Radio Science, 29*, 395–405. https://doi.org/10.1029/93RS01669

Husin, A., Abdullah, M., & Momani, M. A. (2011). Observation of medium-scale traveling ionospheric disturbances over Peninsular Malaysia based on IPP trajectories. *Radio Science, 46*, R2018. https://doi.org/10.1029/2010RS004408

Jacobson, A.R., Carlos, R.C., Massey. R.S., Wu, G. (1995). Observations of traveling ionospheric disturbances with a satellite-beacon radio interferometer: seasonal and local time behavior. *Journal of Geophysical Research*, *100*, 1653–1665.

Jonah, O.F. (2017). A Study of Daytime MSTIDS over Equatorial and Low Latitude Regions during Tropospheric Convection: observations and simulations, the graduate course in space geophysics. Ph.D. thesis, national institute for space research (INPE), Sao Paulo, Brazil. http://www.inpe.br/posgraduacao/ges/arquivos/teses/tese_olusegun_jonah_2017.pdf. Accessed 14 Sept 2021.

Jonah, O. F., Kherani, E. A., & De-Paula, E. R. (2016). Observation of TEC perturbation associated with medium scale traveling ionospheric disturbance and possible seeding mechanism of atmospheric gravity wave at a Brazilian sector. *Journal of Geophysical Research: Space Physics, 121*, 2531–2546. https://doi.org/10.1002/2015JA022273

Jonah, O. F., Zhang, S., Coster, A. J., Goncharenko, L. P., Erickson, P. J., Rideout, W., de Paula, E. R., & de Jesus, R. (2020). Understanding Inter-Hemispheric Traveling Ionospheric Disturbances and Their Mechanisms. *Remote Sens., 12*, 228.

Kelley, M. C., & Miller, C. A. (1997). Electrodynamics of mid-latitude spread. F3 Electrohydrodynamic waves? A new look at the role of electric fields in thermospheric wave dynamics. *Journal of Geophysical Research, 102*, 1139–1547.

Klobuchar, J. A. (1996). Ionospheric effects on GPS. In B. W. Parkinson & J. J. Spilker (Eds.), *Global positioning system: Theory and application*, (vol 1, pp 485–516) American Institute of Aeronautics and Astronautics.

Kotake, N., Otsuka, Y., Ogawa, T., Tsugawa, T., & Saito, A. (2007). Statistical study of medium-scale traveling ionospheric disturbances observed with the GPS networks in Southern California. *Earth, Planets and Space, 59*, 95–102. https://doi.org/10.1186/BF03352681

Koucká Knížová, P., Laštovička, J., Kouba, D., Mošna, Z., Podolská, K., Potužníková, K., Šindelářová, T., Chum, J., Rusz, J. (2021). Ionosphere influenced from lower-lying atmospheric regions. *Frontiers in Astronomy and Space Sciences*, *8*, 651445. https://doi.org/10.3389/fspas.2021.651445.

MacDougall J., Li G., Jayachandran P.T. (2009a). Traveling ionospheric disturbances near London. *Journal of Atmospheric and Solar-Terrestrial Physics*, *71*, 2077–2084. https://doi.org/10.1016/j.jastp.2009.09.016..

Mannucci, A., Wilson, B., Yuan, D., Ho, C., Lindqwister, U., & Runge, T. (1998). A global mapping technique for GPS-derived ionospheric total electron content measurements. *Radio Science*, *33*(3), 565–582.

Miller, E. S., Kil, H., Makela, J. J., Heelis, R. A., Talaat, E. R., & Gross, A. (2014). Topside signature of medium-scale traveling ionospheric disturbances. *Annales Geophysicae, 32*, 959–965. https://doi.org/10.5194/angeo-32-959-2014

Ngwira, C.M., Klenzing, J., Olwendo, J., D'ujanga, F.M., Stoneback, R., Baki, P. (2013). A study of intense ionospheric scintillation observed during a quiet day in the East African low-latitude region. *Radio Science*, *48*, 396–405. https://doi.org/10.1002/rds.20045.

Norsuzila, Y., Abdullah, M., Ismail, M., & Zaharim, A. (2009). Model validation for total electron content (TEC) at an equatorial region. *European Journal of Scientific Research, 28*(4), 642–648.

Ogawa, T., Igarashi, K., Aikyo, K., & Maeno, H. (1987). NNSS Satellite observations of medium-scale traveling ionospheric disturbances at southern high-latitudes. *Journal of Geomagnetism and Geoelectricity, 39*(12), 709–721.

Oinats, A. V., Nishitani, N., & Ponomarenko, P. (2016). Statistical characteristics of medium-scale traveling ionospheric disturbances revealed from the Hokkaido East and Ekaterinburg HF

radar data. *Earth Planet and Space*. https://doi.org/10.1186/s40623-016-0390-8

Oluwadare, T.S., Thai, C.N., Akala, A.O., Heise, S., Alizadeh, M., & Schuh, H. (2019). Characterization of GPS-TEC over African equatorial ionization anomaly (EIA) region during 2009–2016. *Advances in Space Research, 63*(1), 282–301. https://doi.org/10.1016/j.asr.2018.08.044.

Otsuka Y, Kotake N, Shiokawa K., Ogawa T, Tsugawa T, Saito A (2011) Statistical Study of Medium-Scale Traveling Ionospheric Disturbances Observed with a GPS Receiver Network in Japan, Aeronomy of the Earth's Atmosphere and Ionosphere, IAGA Special Sopron Book Series, Vol. 2, Part 3, 291–299, doi:https://doi.org/10.1007/978-94-007-0326-1 21, 2011

Otsuka, Y., Onoma, F., Shiokawa, K., Ogawa, T., Yamamoto, M., & Fukao, S. (2007). Simultaneous observations of nighttime medium-scale traveling ionospheric disturbances and E region field-aligned irregularities at mid-latitude. *Journal of Geophysical Research, 112*, A06317. https://doi.org/10.1029/2005JA011548

Otsuka, Y., Suzuki, K., Nakagawa, S., Nishioka, M., Shiokawa, K., & Tsugawa, T. (2013). GPS observations of medium-scale traveling ionospheric disturbances over Europe. *Annales Geophysicae, 31*, 163–172.

Paulino, I., Moraes, J. F., Medeiros, A. F., Vadas, S. L., Wrasse, C. M., & Takahashi, H. (2016). Periodic waves in the lower thermosphere observed by OI 630 nm airglow images. *Annales Geophysicae, 34*(2), 293–301. https://doi.org/10.5194/angeo-34-293-2016

Perkins, F. (1973). Spread F and ionospheric currents. *Journal of Geophysical Research, 78*, 218–226. https://doi.org/10.1029/JA078i001p00218

Thome, G. D. (1964). Incoherent scatter observations of traveling ionospheric disturbance. *Journal of Geophysical Research, 69*, 4047–4049.

Trinh, Q. T., Ern, M., Doornbos, E., Preusse, P., & Riese, M. (2018). Satellite observations of middle atmosphere-thermosphere vertical coupling by gravity waves. *Annales Geophysicae, 36*(2), 425–444. https://doi.org/10.5194/angeo-36-425-2018

Tsuda, T. (2014). Characteristics of atmospheric gravity waves observed using the MU (Middle and Upper atmosphere) radar and GPS (Global Positioning System) radio occultation. *Proceedings of the Japan Academy. Series b, Physical and Biological Sciences, 90*(1), 12–27. https://doi.org/10.2183/pjab.90.12

Tsugawa, T., Kotake, N., Otsuka, Y., & Saito, A. (2006). Medium-scale traveling ionospheric disturbances observed by GPS receiver network in Japan: A short review. *GPS Solutions, 11*, 139–144. https://doi.org/10.1007/s10291-006-0045-5

Tsugawa, T., Otsuka, Y., Coster, A. J., & Saito, A. (2007). Medium-scale traveling ionospheric disturbances detected with dense and wide TEC maps over North America. *Geophysical Research Letters, 34*, L22101. https://doi.org/10.1029/2007GL031663

Vadas, S. L., & Azeem, I. (2021). Concentric Secondary Gravity Waves in the Thermosphere and Ionosphere over the continental United States on March 25–26, 2015 from Deep Convection. *Journal of Geophysical Research: Space Physics, 126*, e2020JA028275. https://doi.org/10.1029/2020ja028275

Vadas, S. L. J., & Liu, A. (2009). Generation of large-scale gravity waves and neutral winds in the thermosphere from the dissipation of convectively generated gravity waves. *Journal of Geophysical Research, 114*, n. A10310. https://doi.org/10.1029/2009JA014108

Vadas, S., Liu, H. L., & Lieberman, R. (2014). Numerical modeling of the global changes to the thermosphere and ionosphere from the dissipation of gravity waves from deep convection. *Journal of Geophysical Research, 119*, 7762–7793. https://doi.org/10.1002/2014JA020280

Vadas, S. L., & Nicolls, M. J. (2012). The phases and amplitudes of gravity waves propagating and dissipating in the thermosphere: Theory. *Journal of Geophysical Research, 117*, A05322. https://doi.org/10.1029/2011JA017426

Valladares, C. E., & Hei, M. A. (2012). Hei Measurement of the characteristics of TID susing small and regional networks of GPS receivers during the campaign of 17–30 July of 2008. *International Journal of Geophysics, 1–14*, 2012.

Wang, L., & Alexander, J. (2009). Gravity wave activity during stratospheric sudden warming in the 2007–2008 Northern Hemisphere winter. *Journal of Geophysical Research*. https://doi.org/10.1029/2009JD011867

Wang, M., Ding, F., & Wan, W. (2007). Monitoring global traveling ionospheric disturbances using the worldwide GPS network during the October 2003 storms. *Earth Planet Space*. https://doi.org/10.1186/BF03352702

Warnant, R. (1998). Detection of irregularities in the total Electron content using GPS measurements - Application to a mid-latitude station. *Acta Geodaetica Et Geophysica Hungarica, 33*(1), 121–128. 1'1'

Warnant, R., & Pottiaux, E. (2000). The increase of the ionospheric activity as measured by GPS. *Earth, Planets and Space, 52*, 1055–1060.

Yeh, K. C., & Liu, C. H. (1969). *Theory of Ionospheric Waves, Department of Electrical Engineering*. University of Illinois at Urbana-Champaign Urbana.

Yue J., Perwitasari S., Xu S., Hozumi Y., Nakamura T., Sakanoi T. (2019). Preliminary dual-satellite observations of atmospheric gravity waves in airglow. *Atmosphere 10*, 650. https://doi.org/10.3390/atmos10110650.

Zhao, B., Wan, W., Liu, L., & Ren, Z. (2009). Characteristics of the ionospheric total electron content of the equatorial ionization anomaly in the Asian-Australian region during 1996–2004. *Annales Geophysicae, 27*, 3861–3873.

(Received April 16, 2021, revised April 3, 2022, accepted April 6, 2022, Published online May 18, 2022)